

Low-temperature thermodynamic properties near the field-induced quantum critical point in $\text{NiCl}_2\text{-4SC}(\text{NH}_2)_2$

Franziska Weickert,^{1,2} Robert K uchler,¹ Alexander Steppke,¹ Luis Pedrero,¹ Michael Nicklas,¹ Manuel Brando,¹ Frank Steglich,¹ Marcelo Jaime,² Vivien S. Zapf,² Armando Paduan-Filho,³ Khaled A. Al-Hassanieh,⁴ Cristian D. Batista,⁴ and Pinaki Sengupta⁵

¹Max-Planck-Institut f ur Chemische Physik fester Stoffe, 01187 Dresden, Germany

²Los Alamos National Laboratory, MPA-CMMS, Los Alamos, New Mexico 87545, USA

³Instituto de Fisica, Universidade de S o Paulo, S o Paulo, Brazil

⁴Los Alamos National Laboratory, Theory Division T4, Los Alamos, New Mexico 87545, USA

⁵School of Physical and Mathematical Sciences, Nanyang Technological University, Singapore 637371

(Received 6 February 2012; published 8 May 2012)

We present a comprehensive experimental and theoretical investigation of the thermodynamic properties: specific heat, magnetization, and thermal expansion in the vicinity of the field-induced quantum critical point (QCP) around the lower critical field $H_{c1} \approx 2$ T in $\text{NiCl}_2\text{-4SC}(\text{NH}_2)_2$. A $T^{3/2}$ behavior in the specific heat and magnetization is observed at very low temperatures at $H = H_{c1}$, which is consistent with the universality class of Bose-Einstein condensation of magnons. The temperature dependence of the thermal expansion coefficient at H_{c1} shows minor deviations from the expected $T^{1/2}$ behavior. Our experimental study is complemented by analytical calculations and quantum Monte Carlo simulations, which reproduce nicely the measured quantities. We analyze the thermal and the magnetic Gr uneisen parameters, which are ideal quantities to identify QCPs. Both parameters diverge at H_{c1} with the expected T^{-1} power law. By using the Ehrenfest relations at the second-order phase transition, we are able to estimate the pressure dependencies of the characteristic temperature and field scales.

DOI: [10.1103/PhysRevB.85.184408](https://doi.org/10.1103/PhysRevB.85.184408)

PACS number(s): 64.70.Tg, 75.40.-s, 65.40.De

I. INTRODUCTION

Bose-Einstein condensation (BEC) has triggered great interest in the last years and was found in a variety of complex many-body systems, such as cold atoms, superfluid helium, or superconductors. By exploiting the Matusbara-Matsuda mapping of $S = 1/2$ spins into hard-core bosons,¹ Batyev showed that the field-induced phase transition between canted XY antiferromagnetic (AFM) ordering and the fully polarized state can also be described as a BEC.² This useful mapping between magnetic systems and dilute gases of bosons can be extended to higher spin values,^{3,4} and it has been successfully exploited first on TiCuCl_3 (Ref. 5) and other quantum magnets.^{6,7}

One material investigated recently is $\text{NiCl}_2\text{-4SC}(\text{NH}_2)_2$,⁸ also known as dichlorotetrakis-thiourea-nickel (DTN). It has a body-centered tetragonal crystal structure with chains of Ni-Cl-Cl-Ni atoms arranged along the crystallographic c direction. DTN enters the XY AFM ordered state between moderate fields of 2 and 12.5 T, if the magnetic field H is applied along c . The magnetic atom in DTN is Ni^{2+} carrying a spin $S = 1$ due to an almost completely quenched orbital momentum. The Hamiltonian for DTN can be written as

$$\mathcal{H} = \sum_{\mathbf{r}\nu} J_\nu \mathbf{S}_{\mathbf{r}} \cdot \mathbf{S}_{\mathbf{r}+\mathbf{e}_\nu} + \sum_{\mathbf{r}} [D(S_{\mathbf{r}}^z)^2 - g\mu_B H S_{\mathbf{r}}^z], \quad (1)$$

where $\nu = \{a, b, c\}$ and \mathbf{e}_ν is the relative vector between nearest neighbors along the ν direction. The magnitude of the dominant single-ion anisotropy D is 8.9 K.⁹ The AFM exchange interactions between neighboring spins are $J_c = 2.2$ K along the chains, and about 10 times smaller, $J_{ab} = 0.18$ K, in the ab plane. The last Zeeman term in Eq. (1) is originated from the applied magnetic field H and the quantization z axis is

chosen along the field direction. The gyromagnetic factor g parallel to the c axis was estimated to be 2.26 by electron spin resonance (ESR) experiments.⁹ Equation (1) is only a minimal Hamiltonian for describing the magnetic properties of DTN. Further contributions, such as dipolar interactions, which break the $U(1)$ symmetry of global rotations along the spin z axis are small, but they become relevant at very low temperatures. Therefore, the critical exponents characteristic of a BEC quantum critical point (QCP) can only be observed if the $U(1)$ symmetry breaking terms are at least one order of magnitude smaller than J_{ab} . At low enough temperatures, one should observe a crossover from the behavior characteristic for BEC QCPs to the one expected for an Ising-type QCP. Investigations of the exact shape of the phase boundary close to H_{c1} and H_{c2} down to 1 mK by detailed ac susceptibility measurements evidenced the universality class of a BEC in DTN.¹⁰ Up to date, this is the solely experimental observation consistent with a field-induced BEC QCP in this material.

The universality class of the QCP can also be determined by measuring the exponents for the power-law dependencies of different thermodynamic quantities as a function of temperature. Table I shows the expected exponents for BEC and Ising-type QCPs in two and three dimensions d .⁷ It is important to note that $d = 3$ is the upper critical dimension for the Ising-type QCP ($D = d + z = 4$), where $z = 1$ is the dynamical exponent and D the effective dimensionality. Therefore, one should expect further logarithmic corrections to the power-law behaviors listed in Table I. In this work, an extensive study of the magnetization $M(H, T)$, specific heat $C(H, T)$, and thermal expansion $\alpha_\nu(H, T)$ close to the critical field H_{c1} gives further strong evidence that DTN belongs to the universality class of BEC.

TABLE I. Temperature dependencies of the thermodynamic quantities: magnetization $M(T)$, thermal expansion $\frac{\Delta L}{L}$, $\alpha(T)$, and specific heat $C(T)$ at the field-induced QCP. The variable d denotes the spatial dimensionality of the system. The exponents of the Ising-type QCP are given for $d = 3$.

	XY AFM order	Ising
$M(H_c, T)$	$T^{d/2}$	T^2
$\frac{\Delta L}{L}(H_c, T)$	$T^{d/2}$	T^2
$\alpha(H_c, T)$	$T^{d/2-1}$	T
$C(H_c, T)$	$T^{d/2}$	T^3

It has been shown recently¹¹ that QCPs can be detected by measuring the divergence of the thermal Grüneisen parameter

$$\Gamma_{\text{th}} = \frac{\alpha \nu}{C} \quad (2)$$

for pressure tuning, and the magnetic Grüneisen parameter

$$\Gamma_{\text{mag}} = -\frac{\partial M / \partial T}{C} \quad (3)$$

for a magnetic field tuned QCP. Both Grüneisen parameters diverge at the QCP like $\Gamma \propto T^{-1/\nu z}$, where ν is the critical exponent that relates the correlation length with the driving parameter of the quantum phase transition (magnetic field in the case of DTN). The effective dimension $D = d + z$ is higher or equal to 4 with $z = 1$ for the Ising-type and $z = 2$ for the BEC-type QCP, and we get $\nu = 1/2$ for both cases. Therefore, $\Gamma \propto T^{-1}$ is expected for a BEC QCP and $\Gamma \propto T^{-2}$ for an Ising-type QCP in agreement with the power laws listed in Table I.

Typical for QCPs is the occurrence of local maxima in the entropy due to enhanced quantum critical fluctuations. This implies a sign change of the thermal expansion coefficient,¹² which is linked to the entropy via the Maxwell relation $\alpha \nu = -\partial S / \partial p$. In the past, the concept of the diverging Grüneisen parameter was used successfully to identify and characterize not only well-understood magnetic QCPs, but also other more puzzling QCPs in intermetallic compounds.¹³

So far, dilatometric properties were used to investigate the quantum critical behavior of only a few quantum magnets. The $d = 3$ coupled spin-dimer system TiCuCl_3 (Ref. 14) and the quasi-one-dimensional spin-ladder compound $(\text{C}_5\text{H}_{12}\text{N})_2\text{CuBr}_4$ (Ref. 15) are two rare examples. These systems show field-induced phase transitions at low temperatures,^{5,16,17} however, investigations of the thermal expansion coefficient α and the Grüneisen ratio Γ_{th} show significant deviations from the expected behavior in both cases. Dilatometric experiments on TiCuCl_3 reveal that while the thermal Grüneisen parameter diverges with the expected power law $1/T$, the individual quantities specific heat C and thermal expansion α fail to follow the predictions.¹⁸ In $(\text{C}_5\text{H}_{12}\text{N})_2\text{CuBr}_4$, the thermal expansion coefficient α_c along the crystallographic c direction shows a weak indication of $1/\sqrt{T}$ divergency and a clear sign change at the lower and upper critical field $H_{c1/c2}$, but a detailed discussion of Γ_{th} is missing.¹⁹ This study of the thermal and magnetic Grüneisen ratios shows that DTN is an excellent candidate to close this

gap of knowledge about dilatometric properties of insulating quantum critical materials.

The paper is organized as follows: In Sec. II, we describe the experimental techniques that we used in static magnetic fields to measure the specific heat, thermal expansion, and magnetization up to 15 T, the approximated model used for the analytical calculations, and the quantum Monte Carlo (QMC) simulations of the thermodynamic quantities. Section III contains a detailed description of the experimental and theoretical results. We continue in Sec. IV with the comparison between experiment and theory and the analysis of the anomalies at the phase boundary via the Ehrenfest relations. Section V summarizes the most important results of our study.

II. METHODS

The preparation of high-quality single crystals is explained elsewhere.²¹ All experiments were conducted, partly down to 30 mK, inside commercial available dilution refrigerators, furnished with superconducting (SC) magnets with maximum fields of up to 15 T. We measured the magnetization with a high-resolution Faraday magnetometer.²² The thermal expansion and magnetostriction experiments were carried out with a high-precision capacitive dilatometer²³ made of CuBe. The dilatometer can be rotated by 90° in order to measure the length change not only parallel but also perpendicular to the applied magnetic field. The specific heat was measured with the compensated heat-pulse technique²⁴ and the data were confirmed by experiments using the dual-slope method²⁵ on the same sample platform. The precise match between both sets of experimental data is remarkable. Additionally, we used the specific-heat setup to perform magnetocaloric effect (MCE) measurements for a precise estimate of the critical field H_{c1} .

The analytical calculations of the various thermodynamic properties were based on the usual expansion in the gas parameter or ratio between the scattering amplitude and the average interparticle distance $\rho^{-1/3}$.²⁶ For this purpose, we mapped the $S^z = 1$ magnetic excitations of the low-field paramagnetic (PM) state into hard-core bosons, where the z component of the magnetization density in the original model $\langle S_{\mathbf{r}}^z \rangle$ is mapped into the particle density ρ . Here, we neglect the contribution to the magnetization of the $S^z = -1$ modes because we are assuming that H is close to H_{c1} and $T \ll \Delta$, with $\Delta \simeq 3$ K being the $H = 0$ spin gap of DTN. We use the expression derived in Ref. 27 for the single-particle dispersion $\omega_{\mathbf{k}} = \omega_{\mathbf{k}}^0 - g\mu_B H$ with

$$\omega_{\mathbf{k}}^0 = \sqrt{\mu^2 + 2\mu s^2 \epsilon_{\mathbf{k}}}. \quad (4)$$

The parameters s^2 and μ are given by the following expressions:

$$s^2 = 2 - \frac{1}{N} \sum_{\mathbf{k}} \frac{\mu + s^2 \epsilon_{\mathbf{k}}}{\omega_{\mathbf{k}}^0}, \quad D = \mu + \frac{\mu}{N} \sum_{\mathbf{k}} \frac{\epsilon_{\mathbf{k}}}{\omega_{\mathbf{k}}^0}. \quad (5)$$

By using the Hamiltonian parameters for DTN estimated in Ref. 9, the resulting values are $s^2 = 0.92$ and $\mu = 10.3$ K. The effective repulsion between bosons in the long-wavelength limit $v_0 = \Gamma_0(\mathbf{Q}, \mathbf{Q})$, with \mathbf{Q} being the ordering wave vector, results from summing the ladder diagrams for the bare

interaction vertex $V_{\mathbf{q}}$ (Ref. 26):

$$\Gamma_{\mathbf{q}}(\mathbf{k}, \mathbf{k}') = V_{\mathbf{q}} - \int_{-\pi}^{\pi} \frac{dp^3}{8\pi^3} \frac{\Gamma_{\mathbf{p}}(\mathbf{k}, \mathbf{k}')}{\omega_{\mathbf{k}+\mathbf{p}} + \omega_{\mathbf{k}'-\mathbf{p}}}, \quad (6)$$

where $V_{\mathbf{q}} = U + 2J_c \cos q_z + 2J_{ab}(\cos q_x + \cos q_y)$ for DTN and $U \rightarrow \infty$ is included to enforce the hard-core constraint. The effective Hamiltonian in the long-wavelength limit $|\mathbf{k} - \mathbf{Q}| \ll 1$ is given by

$$\mathcal{H}_{\text{eff}} = \sum_{\mathbf{k}} (\epsilon_{\mathbf{k}} - \mu) a_{\mathbf{k}}^{\dagger} a_{\mathbf{k}} + \frac{v_0}{2N} \sum_{\mathbf{k}, \mathbf{k}', \mathbf{q}} a_{\mathbf{k}+\mathbf{q}}^{\dagger} a_{\mathbf{k}'-\mathbf{q}}^{\dagger} a_{\mathbf{k}} a_{\mathbf{k}'}, \quad (7)$$

where N is the total number of lattice sites and the operator $a_{\mathbf{k}}^{\dagger}$ ($a_{\mathbf{k}}$) creates (annihilates) a boson with momentum \mathbf{k} . $\epsilon_{\mathbf{k}}$ is obtained by taking the long-wavelength limit of $\omega_{\mathbf{k}}$:

$$\epsilon_{\mathbf{k}} = \frac{k_z^2}{2m_{cc}^*} + \frac{(k_x^2 + k_y^2)}{2m_{aa}^*} \quad (8)$$

with

$$\frac{1}{m_{vv}^*} = \left. \frac{\partial^2 \omega_{\mathbf{k}}}{\partial k_v^2} \right|_{\mathbf{k}=\mathbf{Q}}. \quad (9)$$

The chemical potential μ is $g\mu_B H - \omega_{\mathbf{Q}}$. After a mean-field treatment of \mathcal{H}_{eff} in the PM phase $H \leq H_{c1}$, the interaction term simply leads to a renormalization of the chemical potential $\mu \rightarrow \tilde{\mu}$, with

$$\tilde{\mu} = \mu - 2v_0\rho \quad (10)$$

and the particle density

$$\rho = \frac{1}{N} \sum_{\mathbf{k}} \langle a_{\mathbf{k}}^{\dagger} a_{\mathbf{k}} \rangle. \quad (11)$$

The resulting quadratic mean-field Hamiltonian can be easily diagonalized, and the various thermodynamic properties are computed by solving the self-consistent condition imposed by Eqs. (10) and (11)

The analytic calculations have been supplemented by large-scale numerical simulations of the microscopic model. We have used the stochastic series expansion (SSE) QMC method to simulate the Hamiltonian (1) on finite-sized lattices using the experimentally determined parameters. The SSE is a finite-temperature QMC technique based on importance sampling of the diagonal matrix elements of the density matrix $e^{-\beta H}$.^{28,29} The use of *operator loop* cluster updates reduces the autocorrelation time for the system sizes. We consider here up to $\approx 2 \times 10^4$ spins to at most a few Monte Carlo sweeps even at the critical temperature.³⁰ This enables us to explore the vicinity of the critical points very efficiently. On the dense temperature grids needed to study the critical region in detail, the statistics of the Monte Carlo results can be significantly improved by the use of a parallel tempering scheme.^{31,32} The implementation of this tempering scheme in the context of the SSE method has been discussed in detail previously,^{33,34} and we follow the one developed in Ref. 34.

QMC estimates for observables of a spatially anisotropic system can depend nonmonotonically on the system size for isotropic lattices. One can instead use anisotropic lattices to more rapidly obtain monotonic behavior of the numerical

results for extrapolating to the thermodynamic limit. Anticipating similar effects in the present model (since $J_a, J_b \ll J_c$), we have studied tetragonal lattices with $L_x = L_y = L_z/4$.

The specific heat has been extracted from the simulation data by the numerical differentiation of the total internal energy of the system, a quantity that is estimated extremely accurately by the SSE method. The temperature dependence of the energy is approximated by a polynomial in T , and the derivative of the polynomial fit is used to estimate the specific heat. Thus, artifacts of discrete numerical differentiation of the raw data are avoided and we yield a relatively noise-free specific-heat curve.

III. EXPERIMENTAL RESULTS

A. Magnetization

Figure 1 shows a comparison of the magnetization M as a function of magnetic field measured perpendicular at $T = 500$ mK (Ref. 20) and parallel at $T = 16$ mK (Ref. 21) to the crystallographic c axis. The latter data nicely reflect the Néel-ordered state in the ab plane with increasing canting along c between 2.1 and 12.6 T followed by saturation. For $H \parallel ab$, the magnetization shows PM behavior with no ordering, approximately following a Brillouin function and saturating at $2.2 \mu_B$ per Ni^{2+} atom around 15 T. In this field direction, the magnetic field increases the size of the spin gap instead of closing it as happens for $H \parallel c$. The inset of Fig. 1 shows the low-field part of the magnetization $H \parallel c$ at 50 mK in greater detail. We observe a linear increase between zero and the lower critical field H_{c1} , which can not be explained with a U(1)-invariant Hamiltonian such as \mathcal{H} , where the magnetization is supposed to be zero at $T = 0$ in the quantum PM region $H \leq H_{c1}$. This effect can not be caused by single-ion impurities, e.g., uncoupled Ni^{2+} moments, because such spins should be

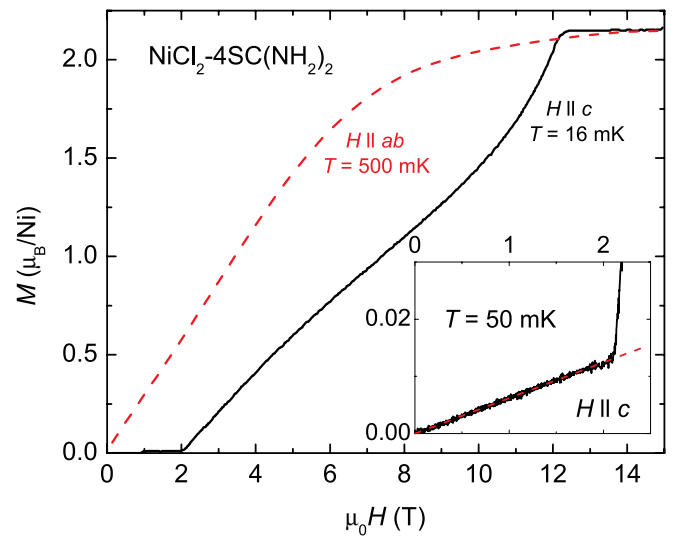


FIG. 1. (Color online) Magnetization M as a function of the magnetic field H of DTN at 16 mK for measurements H parallel (solid line, Ref. 21) and perpendicular to the crystallographic c direction at 500 mK (dashed line, Ref. 20). The inset shows new results of the magnetization at 50 mK in low fields up to 2.5 T and a linear fit (dashed line) to the data.

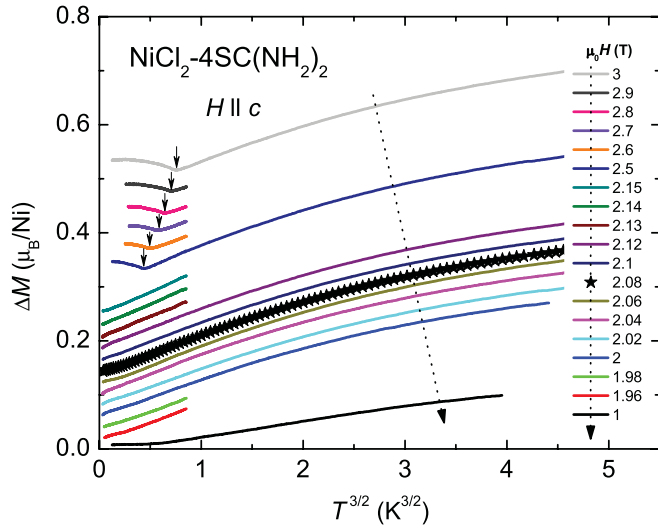


FIG. 2. (Color online) Corrected magnetization ΔM versus $T^{3/2}$ for magnetic fields $H \parallel c$ between 1 and 3 T. The magnetization at the critical field $\mu_0 H_{c2} = 2.08$ T is labeled with stars. Data above 1 T are shifted vertically by $0.02 \mu_B$ per Ni atom for better visualization. Arrows indicate the phase transition into the XY AFM state.

fully polarized for magnetic fields well below the lower critical field $H \ll H_{c1}$. Instead, we conclude that the linear slope (dotted line) is caused by a misalignment of the sample, which gives a contribution $M(H \perp c)$ to the magnetization. From the value of the susceptibility compared to data for $H \perp c$, we estimate a misalignment of less than 1.2° .

Furthermore, we measured the magnetization for $H \parallel c$ near H_{c1} and in the temperature range $0.1 \text{ K} \leq T \leq 0.5 \text{ K}$ (data not shown) to extrapolate the phase boundary for $T \rightarrow 0$.¹⁰ We obtain a critical field H_{c1} of 2.08 T. It is important to note that this value depends on the specific conditions under which the sample is mounted in the experimental setup. The slightly higher value of H_{c1} in the magnetization compared to the specific heat and thermal expansion $L \parallel c$ values (see data below) supports the assumption of small sample misalignment because angular-resolved measurements of the magnetostriction have shown that H_{c1} increases with increasing angle between the field direction and the crystallographic c axis.²⁰

The small PM contribution M_{PM} to the magnetization made it necessary to refine the $M(T)$ data as a function of temperature for $H \parallel c$. Figure 2 shows the corrected values $\Delta M(T) = M - M_{\text{PM}}$ plotted versus $T^{3/2}$ for a variety of different magnetic fields $1 \text{ T} < \mu_0 H < 3 \text{ T}$. The magnetization is exponentially suppressed at low temperatures inside the quantum PM state ($\mu_0 H = 1 \text{ T}$) and develops a $T^{3/2}$ behavior when approaching the critical field $H_{c1} = 2.08 \text{ T}$ in agreement with the expected behavior for a BEC QCP in three dimensions. The entrance into the XY AFM state well above H_{c1} is marked with a dip in the magnetization (arrows in Fig. 2). Below the minimum inside the AFM phase, the magnetization increases with a power law for decreasing temperature.

B. Specific heat

We estimate the critical field H_{c1} by MCE measurements (data not shown) following the analysis of the highest slope

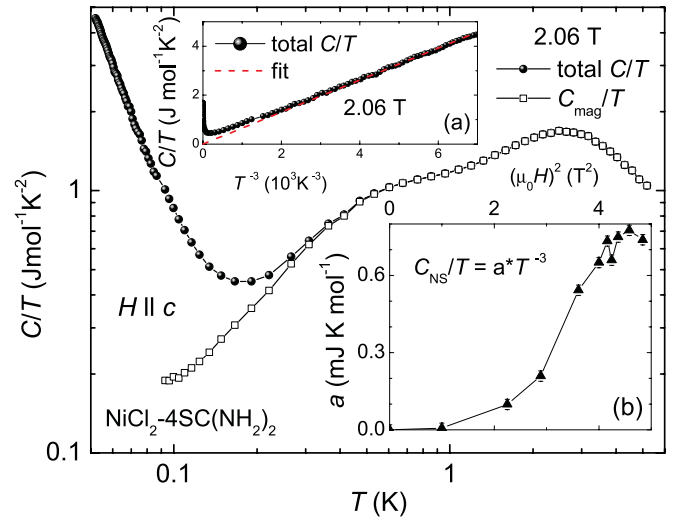


FIG. 3. (Color online) Main panel: total specific heat C/T as a function of temperature T at the critical field $H_{c1} = 2.06 \text{ T}$ (filled dots) and the resulting C_{mag}/T (open squares) after subtraction of the nuclear Schottky (NS) contribution at low temperatures. Inset (a) shows the data of the main panel as C/T versus T^{-3} to illustrate the NS specific heat as indicated by a dashed line. The prefactor of the NS specific heat $C_{\text{NS}}/T = aT^{-3}$ is plotted in inset (b) versus H^2 . It does not follow the expected H^2 field dependence.

($\partial T/\partial H$) of the temperature during field scans³⁵ and find a value $H_{c1} = 2.06 \text{ T}$ in the specific-heat experimental setup.

The specific-heat curve of DTN contains three contributions: nuclear Schottky (NS), magnetic Schottky (MS), and quantum-critical (QC) contributions. Each of these dominates in different regions of the H - T phase diagram. The specific heat caused by phonons can be neglected in the temperature range below 5 K. The NS contribution is difficult to master in this material because it originates from several nuclei (H, N, Cl) generating a huge fraction of the specific heat at temperatures below 0.1 K (see, e.g., in Fig. 3 the measurement at 2.06 T). In addition, the effective magnetic field (sum of the external field and the field generated by the ordered moments) becomes rather high in the AFM ordered state above H_{c1} . This increases the splitting of the nuclear energy levels further and the Schottky anomaly becomes very big. The inset (a) of Fig. 3 demonstrates the way we subtracted the NS contribution from the original specific heat at the critical field $\mu_0 H = 2.06 \text{ T}$. We fit the data between 80 and 50 mK as $C/T = aT^{-3}$, which is a good approximation for the high-temperature behavior of the Schottky anomaly.³⁶ The prefactor a for the NS specific heat is given as a function of magnetic field in the inset (b) of Fig. 3. The prefactors for different nuclei should be additive, $a = \sum a_i$, for the case that all the different nuclear energy levels are in the high-temperature limit ($k_B T \gg \Delta_{\text{nuclear}}$). Because the Zeeman splitting is linear in magnetic field, $a(H)$ should obey a H^2 dependence for $H < H_{c1}$. This is not observed in DTN and presently not understood.

The insulating behavior of DTN is challenging for specific-heat experiments because no free electrons contribute to the thermal conductivity. Heat is carried only by magnetic excitations and by phonons, whereas the phonon contribution is negligibly small in the temperature range below 1 K.

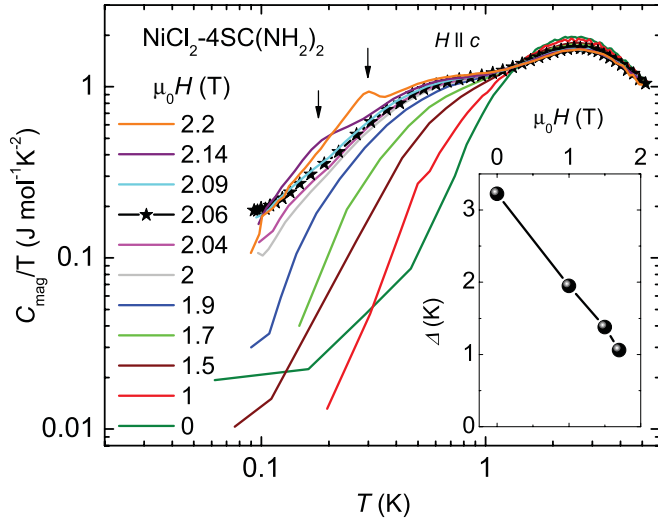


FIG. 4. (Color online) Magnetic specific heat C_{mag}/T as a function of temperature T for magnetic fields between 0 and 2.2 T in a double-log scale. The arrows indicate the AFM phase transition for fields $H > H_{c1}$. The critical field obtained from MCE experiments is 2.06 T. The inset shows the energy gap between 0 and 1.7 T, estimated from the exponential temperature increase of the magnetic specific heat at low temperatures.

Therefore, the different thermodynamic subsystems (nuclear spins, magnetic moments, lattice) are only poorly coupled to each other at low temperatures. This causes an out-of-equilibrium state of the sample at very low temperatures. Thus, we only include data above 80 mK in our analysis.

Figure 4 shows the magnetic specific heat $C_{\text{mag}}/T = C/T - C_{\text{NS}}/T$ in a double-logarithmic display after the subtraction of the nuclear Schottky contribution C_{NS} between 0 and 2.2 T. The broad maximum around 2.5 K in the zero-field measurement is caused by the thermal population of the $S^z = \pm 1$ excited states that are a rather broad band due to dispersion caused by the exchange interactions.³⁵ This dispersion is also responsible for the only slightly shift of the maximum to lower temperatures with higher magnetic fields. For small fields, the specific-heat data can be fitted with an exponential function $\exp(-\frac{\Delta}{k_B T})$ in the low-temperature limit, allowing us to extract the spin gap Δ . The inset of Fig. 4 shows the gap values, estimated from the experimental data. They decrease linearly from 3.22 K down to 1 K when H varies between 0 and 1.7 T, whereas the zero-field value is in close accordance with previous susceptibility results of 3.3 K.³⁷ Below 1.7 T, the temperature range for exponential behavior is too small for reliable data fitting. From the zero-field gap $\Delta = 3.22$ K, we can estimate the critical field

$$H_{c1} = \frac{k_B \Delta}{g \mu_B}, \quad (12)$$

where the gap closes ($k_B = 1.380 \times 10^{-23} \text{ JK}^{-1}$ and $\mu_B = 9.274 \times 10^{-24} \text{ JT}^{-1}$). The calculated value $H_{c1} = 2.12$ T matches the experimental values summarized in Table II within 5%. The arrows in Fig. 4 indicate the anomalies caused by the phase transition into the XY AFM state in the 2.14- and 2.2-T measurements.

TABLE II. Critical field H_{c1} estimated by different experimental methods and setups.

Thermodynamic quantity	H_{c1} (T)
Magnetization $M(H, T)$	2.08
Magnetocaloric effect (MCE)	2.06
Magnetostriction $\Delta L \parallel c$	2.02
Magnetostriction $\Delta L \perp c$	2.08

C. Thermal expansion

The linear thermal expansion coefficient

$$\alpha_i = \frac{1}{L_0} \frac{\partial \Delta L_i}{\partial T} \quad (13)$$

is defined as the temperature derivative of the length change ΔL_i along a certain crystallographic direction i . In tetragonal systems, such as DTN, the volumetric expansion can be calculated from the linear coefficients

$$\alpha_V = 2\alpha_a + \alpha_c \quad (14)$$

along the crystallographic a and c directions.

The main panel of Fig. 5 shows α_c for $H \parallel c$ between 0 and 5.5 T. For measurements well above H_{c1} , the transition into the ordered phase is indicated by a distinct anomaly, marked with arrows. In the temperature range up to 5 K, no significant contribution from the lattice is observed. In zero field, α_c shows a rather broad minimum that shifts to lower temperatures in higher fields and can be attributed to the thermal population of energetically higher spin states $S^z = \pm 1$, similar to the maximum in the specific heat. In zero field, these spin states are equally occupied because they have the same energy. The largest AFM exchange along the c axis leads to the

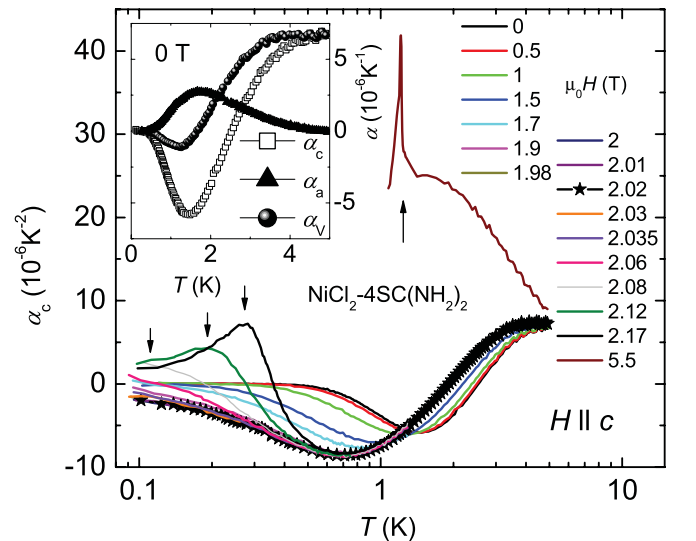


FIG. 5. (Color online) Linear thermal expansion coefficient α_c measured along the crystallographic c axis ($H \parallel c \parallel \Delta L_c$) as a function of the temperature T between 0 and 5.5 T, including the critical field $H_{c1} = 2.02$ T. Arrows mark the phase transition into the AFM ordered state. The inset displays in addition to α_c the coefficient α_a ($H \parallel c$, ΔL_a) and the calculated volumetric coefficient $\alpha_V = 2\alpha_a + \alpha_c$ for 0 T.

dominant magnetostrictive effect. Since the PM ground state is a product of $S^z = 0$ state to a good approximation, the thermal excitation of $S^z = \pm 1$ states increases the nearest-neighbor XY AFM correlations along the c axis ($\mathbf{S}_r \cdot \mathbf{S}_{r+e_c}$). This increase leads to an attractive magnetostrictive force between nearest-neighbor ions along the c axis that shrinks the lattice as the temperature increases from zero. On the other hand, the magnetostrictive force disappears at high enough temperature because $\langle \mathbf{S}_r \cdot \mathbf{S}_{r+e_c} \rangle \rightarrow 0$ for $T \rightarrow \infty$, implying that ΔL_c must have a minimum at a finite temperature where α_c changes sign. This expected behavior is fully consistent with the experimental results shown in Fig. 5. The critical field for the thermal expansion measurements was estimated by detailed magnetostriction measurements, whereas the magnetostriction coefficient

$$\lambda_i = \frac{1}{\mu_0 L_0} \frac{\partial \Delta L_i}{\partial H} \quad (15)$$

is defined as the magnetic field derivative of the length change along the i direction. The analysis of the data (not shown) gives $H_{c1} = 2.02$ T for ΔL_c and $H_{c1} = 2.08$ T for ΔL_a . The difference in the critical field values can be attributed to the application of small pressure on the sample during the experiment (see also Sec. IV D).

The inset of Fig. 5 compares α_c , α_a , and α_V for the zero-field measurement. Between 5 and 3 K, the thermal expansion is dominated by the length change along the c direction, $\alpha_c > 0$, $\alpha_a = 0$, because of the quasi-one-dimensional nature of the magnetic interactions in this temperature range. In the temperature range below 3 K, the thermal expansion coefficient α_c is negative and has the minimum that is expected because the curve $\alpha_c(T)$ must change sign at a finite temperature. In contrast, the thermal expansion coefficient in the plane α_a is positive for $T < 3$ K with a maximum at the temperature $T = T_m$ where the minimum occurs in α_c . Calculating α_V via Eq. (14) reveals that the thermal expansion coefficients α_a and α_c strongly compensate each other and that the volume coefficient changes much less than the individual α_i values.

IV. DISCUSSION

A. Critical field H_{c1}

The values for the lower critical field H_{c1} , estimated individually for the different experimental quantities, are summarized in Table II. The values vary by ± 30 mT around 2.05 T. This difference can be attributed to the application of small pressure on the sample during the experiment. The spring-loaded capacitive dilatometer for thermal expansion and magnetostriction measurements can intrinsically apply a small amount of uniaxial pressure along the measured sample length. The misalignment of the crystal orientation out of $H \parallel c$ indicated by the magnetization experiments is another reason for variations in H_{c1} .

B. Comparison theory: Experiment

Figure 6 shows a comparison between the experimental magnetization (symbols) at the critical field and analytical calculations (solid line) and QMC simulations (dashed line).

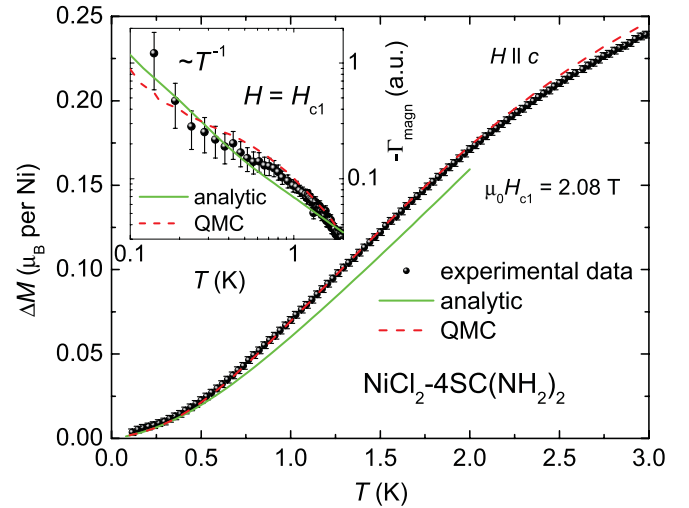


FIG. 6. (Color online) Experimental magnetization $\Delta M(T)$ versus temperature T (symbols) at the critical field $\mu_0 H = 2.08$ T applied along the crystallographic c direction of DTN. The dashed line represents QMC results, whereas the solid line indicates the analytic calculations. The symbols in the inset show the magnetic Grüneisen parameter Γ_{mag} estimated from the data of the main panel and the specific-heat values shown in Fig. 4. Dashed and solid lines represent QMC and analytical results, respectively.

We observe that the QMC and analytic results agree with the experimental data within the error bars below 0.5 K. A $T^{3/2}$ behavior is expected below 0.3 K for the BEC universality class, in contrast to T^2 dependence of an Ising-type QCP. While the analytic calculation is only valid at low temperatures (or low density of bosons), the QMC results remain valid at any temperature. This is the reason why the QMC results are in very good agreement with the experimental data up to 2.2 K.

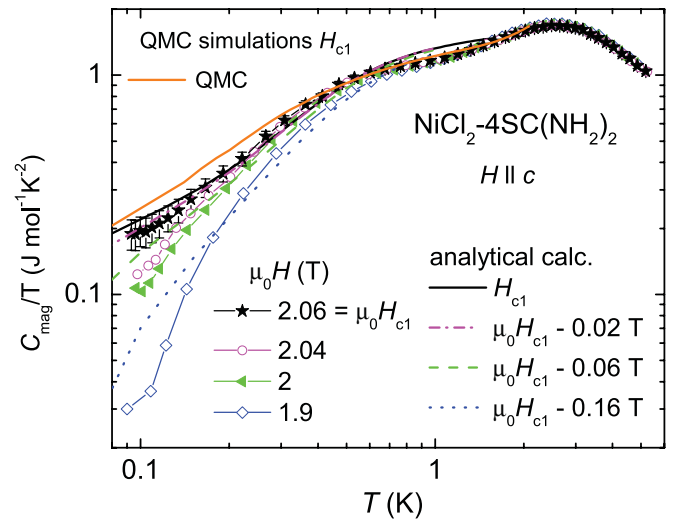


FIG. 7. (Color online) Magnetic specific heat as C_{mag}/T as a function of temperature T at the critical field $H_{c1} = 2.06$ T (stars), at 2.04 T (open circles), 2 T (filled triangles), and 1.9 T (open diamonds) compared with QMC results at H_{c1} (solid line) and with analytical calculations (dashed, dotted lines) at H_{c1} and for fields below the critical field.

Figure 7 shows the experimental data of the specific heat $C_{\text{mag}}/T(T)$ (symbols) at and slightly below the critical field H_{c1} , compared with data of analytic calculations (broken lines) and QMC simulations (solid line) in a double-logarithmic display. The experimental data exhibit a \sqrt{T} dependence in the low-temperature limit at the critical field, in agreement with mean-field calculations and QMC simulations, which is characteristic for the three-dimensional BEC universality class. We observe that the experimental data agree well within error bars with the analytic results down to the lowest temperatures, whereas there is a slight deviation of the QMC results below 0.3 K. This discrepancy is most likely due to a small error in the numerical determination of the critical field H_{c1} . A linear temperature dependence of the specific heat $C_{\text{mag}}/T(T)$ is expected for an Ising-type QCP, which we can exclude from our measurements. The broad Schottky maximum around 2.5 K in the experimental data originating from the population of $S^z = \pm 1$ excited spin states can only be reproduced by the QMC simulations because they remain valid up to arbitrarily high temperatures. Seen in the experimental data as well as in the QMC results is the crossover from three dimensional ($C/T \sim T^{1/2}$) to one dimensional ($C/T \sim T^{-1/2}$) behavior of the specific heat at higher temperatures for the measurement at H_{c1} . The change of slope is marked with a broad hump around 0.5 K. Note that the one-dimensional temperature dependence overlaps with the above-mentioned Schottky contribution to the specific heat.

For $H < H_{c1}$ measurements, the analytical curves as well as the experimental values lie below the specific-heat data at the critical field. They grow smaller as the distance from H_{c1} increases. This observation confirms the correct estimation of the value $H_{c1} = 2.06$ T for the critical field in the MCE measurements. Furthermore, Fig. 7 shows nice agreement between analytical predictions and experimental data at low temperatures for all shown fields. Deviations seem to be larger for $H < H_{c1}$, but this is an effect of the double-logarithmic display.

In presence of Ising-type anisotropy, the gap should reopen inside the AFM phase. We do not observe any exponential temperature dependence in the measurements for fields above H_{c1} in Fig. 4, namely, 2.09, 2.14, and 2.2 T. This, however, could also be due to (i) lack of data at temperatures below 80 mK and (ii) the onset of the phase transition seen as a broad anomaly in the specific heat.

Before we discuss the scaling behavior of the thermal expansion coefficient at the critical field, let us have a closer look at the length change $\Delta L_c/L$, which is shown in Fig. 8 along with results from QMC simulations. The inset (a) of Fig. 8 shows the experimental length at the critical field after the subtraction of the data in 0 T in order to separate quantum critical from the noncritical magnetic contributions of the sample. The same procedure was done for QMC data. In QMC simulations, $\Delta L_c/L$ at H_{c1} is obtained from the estimation of the spin-spin correlator (SSC), $\langle \mathbf{S}_r \cdot \mathbf{S}_{r+e_i} \rangle$,³⁸ and optionally additional terms. The main panel of Fig. 8 shows the comparison between the experimental data and QMC simulations. The qualitative features are well reproduced by the expectation value of the SSC for temperatures above 0.3 K. The scaling factor between experiment and theory is 1.85×10^{-4} . $\Delta L_c/L$ follows a T^γ power law with γ between 2

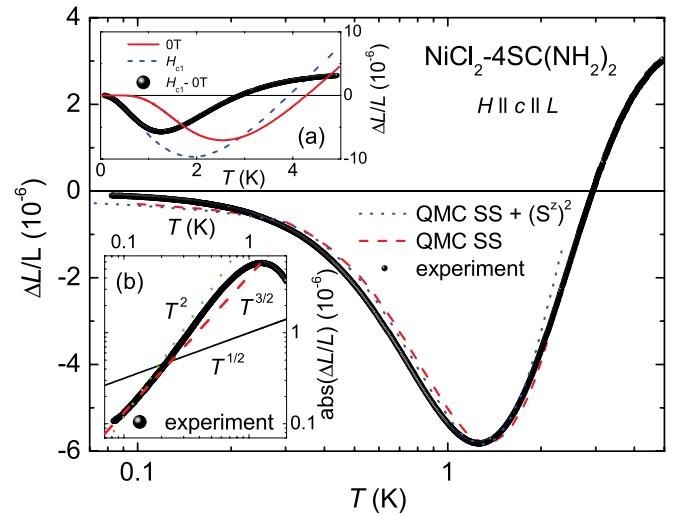


FIG. 8. (Color online) The main panel shows the normalized length change $\Delta L/L$ (symbols) as a function of the temperature T of DTN for $H \parallel c \parallel L_c$ at the critical field $H_{c1} = 2.02$ T in a semilogarithmic display. The experimental data are compared with QMC calculations, where the spin-spin correlator (SSC) (dashed line) and the SSC together with the $(S^z)^2$ term (dotted line) are taken into account. The inset (a) shows the experimental data at zero field (solid), the critical field $H_{c1} = 2.02$ T (dotted line), and the difference $\Delta L_c/L(H_{c1}) - \Delta L_c/L(0)$ (symbols). In inset (b), the absolute values $\Delta L/L$ (symbols) are plotted as a function of T in comparison with $\sim T^{1/2}$ (solid), $\sim T^{3/2}$ (dashed), and $\sim T^2$ (dotted line) temperature dependence.

and 3/2 as illustrated in inset (b) of Fig. 8. This result is in close accordance with the expected BEC behavior of $\sim T^{3/2}$. The discrepancy between experimental data and QMC simulations below 0.3 K can be attributed to additional contributions to $\Delta L_c/L$ besides the SSC. However, an additional consideration of a $\langle (S_r^z)^2 \rangle$ term that is expected from symmetry arguments does not improve the agreement significantly. Therefore, the origin of this discrepancy remains unclear at the present level of analysis.

Figure 9 summarizes the volumetric thermal expansion coefficient divided by the temperature α_V/T for fields at and close to the QCP. Note that according to Eq. (14) different critical values H_{c1} were considered for α_a and α_c and taken into account for the estimation of α_V . We find that at H_{c1} the values α_V/T have a weak but finite temperature dependence (solid line) meaning that the thermal expansion coefficient α_V diverges as expected at the QCP. For magnetic fields $H \leq H_{c1}$, the low-temperature values α_V/T show similar behavior.

In general, pressure p and magnetic field H are equivalent parameters of the free energy $F(p, H)$ in close vicinity to the critical field $|H_{c1} - H| \ll H_{c1}$. Therefore, thermodynamic quantities derived from pressure and field dependencies can be converted

$$\frac{\partial}{\partial p} = \Omega \frac{\partial}{\partial H} \quad (16)$$

by multiplication with the prefactor $\Omega = \partial H_{c1}/\partial p$, which is the hydrostatic pressure dependence of the critical field H_{c1} .

Equation (16) implies that the compressibility $\kappa = \partial^2 F/\partial p^2$ is proportional to the magnetic susceptibility that

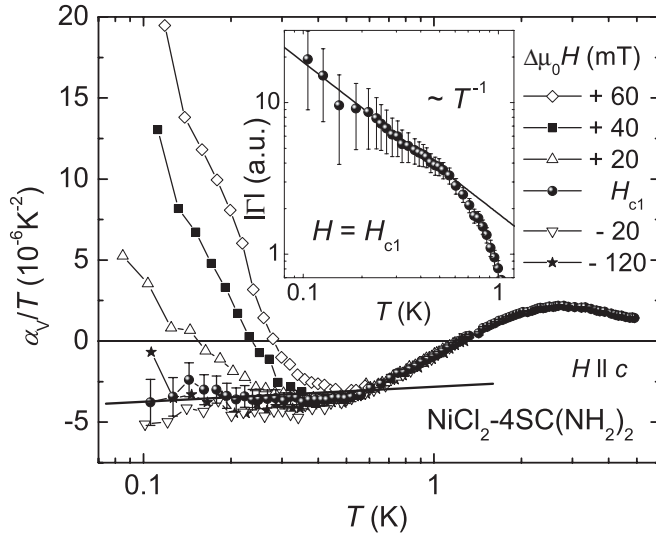


FIG. 9. The volume thermal expansion coefficient divided by T is presented for fields close to the critical fields as a function of temperature T in a semilogarithmic plot for DTN with field direction $H \parallel c$. The inset shows the absolute value of the thermal Grüneisen parameter $\Gamma_{\text{th}} = \alpha_V/C$ at the critical field H_{c1} . The solid line in the inset illustrates T^{-1} behavior.

is a step function of the magnetic field at H_{c1} and is shown in Fig. 10. Therefore, κ increases rapidly at H_{c1} and leads to a softening of the crystal lattice, recently demonstrated experimentally on DTN by ultrasound experiments.³⁹ Considering this, we speculate that the huge change in the lattice properties is responsible for the deviation of α_V from the exact behavior of a BEC. Similar crystal softening as a precursor for quantum criticality was, e.g., also observed at the metamagnetic transition in CeRu_2Si_2 .⁴⁰

The thermal expansion coefficient α_V for fields above H_{c1} shows the clear onset of the phase transition with positive values $\alpha_V > 0$ in Fig. 9.

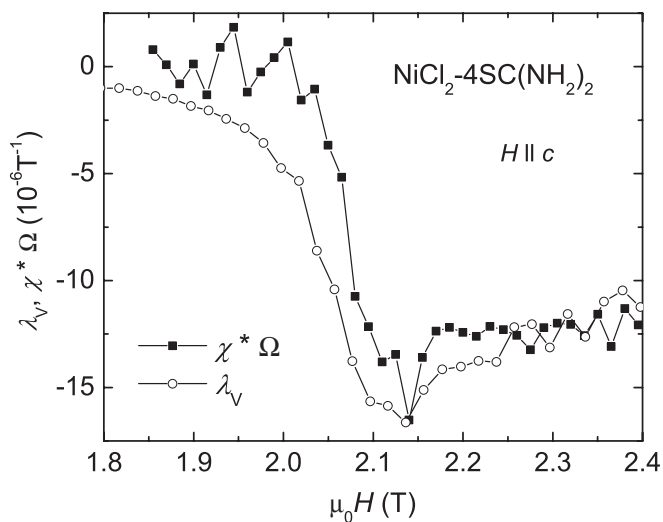


FIG. 10. Volume magnetostriction coefficient λ_V and susceptibility $\chi = \mu_0^{-1} \partial M / \partial H$ at 0.1 K of DTN. The susceptibility is scaled by the hydrostatic pressure dependence of the critical field Ω estimated from the Ehrenfest relations.

C. Grüneisen parameter

The magnetic Grüneisen parameter Γ_{mag} is given in the inset of Fig. 6 and compared with theoretical data of the QMC simulation and the analytical calculations. In the temperature range below 0.3 K, the experimental Γ_{mag} shows the onset of divergence, as expected for a QCP. As far as it is observable in the low-temperature limit, Γ_{mag} follows the theoretical prediction $\sim T^{-1}$ because the magnetization and specific heat obey the expected behavior individually. For the thermal Grüneisen parameter Γ_{th} , shown in the inset of Fig. 9, a T^{-1} behavior is found as well for temperatures below 0.6 K. These observations are fully in agreement with the universality class of a BEC QCP.

D. Ehrenfest relations

The anomalies at the phase boundaries observed in the thermal expansion coefficient α_i , the specific heat C , the magnetostriction coefficient λ_i , and the magnetization M allow us to obtain the pressure dependence of (i) the transition temperature T_N ,

$$\frac{\partial T_N}{\partial p_i} = V_m T_N \frac{\Delta \alpha_i}{\Delta C_p}, \quad (17)$$

and of (ii) the critical field H_{c1} ,

$$\frac{\partial H_{c1}}{\partial p_i} = V_m \frac{\Delta \lambda_i}{\Delta \chi}, \quad (18)$$

by the Ehrenfest relations, which hold at phase transitions of second order. Equations (17) and (18) are valid for uniaxial as well as hydrostatic pressure, dependent if the linear or volume coefficients λ_i or α_i are used in the analysis.

We find $\partial T_N / \partial p_c = 18.5 \text{ K GPa}^{-1}$ at $H = 2.2 \text{ T}$ for uniaxial pressure applied along the crystallographic c direction. This value is rather high, even compared to TiCuCl_3 , which already exhibits a huge value of several Kelvin per GPa dependent on the considered field range.⁴¹ Direct measurements of the thermal expansion ΔL_a are currently not available, however, from measurements in small magnetic fields $H < H_{c1}$, we expect a negative uniaxial pressure dependence $\partial T_N / \partial p_a$, which should partially cancel the value (18.5 K GPa^{-1}) along c , leading to a smaller but positive hydrostatic value. Similar behavior was observed in TiCuCl_3 .⁴¹

The pressure dependence of the critical field $\partial H_{c1} / \partial p_i$ could be obtained at 0.1 K for both directions c and a . Because of a negative jump $\Delta \lambda_c$ in the magnetostriction coefficient at H_{c1} (data not shown), the value $\partial H_{c1} / \partial p_c = -6.76 \text{ T GPa}^{-1}$ is negative. In contrast, $\partial H_{c1} / \partial p_a = 1.84 \text{ T GPa}^{-1}$ is positive and the resulting hydrostatic pressure dependence, which is equivalent to the prefactor Ω in Eq. (16), adds to -3.07 T GPa^{-1} . The correct estimate of Ω can be proved by a comparison of λ_V with the magnetic susceptibility χ measured at 0.1 K. Both thermodynamic quantities are linked via Eq. (16) and it follows

$$\lambda_V = \frac{\partial^2 F}{\partial p \partial H} = \Omega \frac{\partial^2 F}{\partial H^2} = \Omega \chi. \quad (19)$$

Figure 10 shows an excellent agreement between the magnetostriction coefficient λ_V and the scaled susceptibility $\Omega \chi$. We conclude from the analysis of the Ehrenfest relations that

the application of uniaxial pressure p_c along the c direction increases the ordering temperature T_N and reduces the critical field H_{c1} . The behavior is opposite for uniaxial pressure along the a direction. The response of DTN to hydrostatic pressure is dominated by the uniaxial pressure dependence along the c axis because this is the direction of the dominant magnetic exchange interaction.

V. SUMMARY

We present a comprehensive experimental and theoretical study of the thermodynamic properties: specific heat, magnetization, and thermal expansion in the vicinity of the field-induced QCP around $H_{c1} \approx 2$ T in $\text{NiCl}_2\text{-}4\text{SC}(\text{NH}_2)_2$. This point marks the entrance into a three-dimensional XY antiferromagnetically ordered state and can be described within the formalism of a BEC of magnons. We find a $T^{3/2}$ low-temperature behavior of the specific heat and the magnetization at H_{c1} that are in agreement with the universality class of a BEC QCP. The thermal expansion coefficient shows a temperature dependence T^γ with $3/2 < \gamma < 2$ for $T \rightarrow 0$, which is in close agreement with expectations for this kind of QCP. QMC simulations nicely reproduce the features observed in the magnetization, specific heat, and thermal expansion over a broad temperature range. Only the low-temperature dependence in the specific heat and thermal expansion deviates due to intrinsic uncertainties in the simulation method. Furthermore,

we analyzed the thermal Γ_{th} as well as the magnetic Grüneisen parameter Γ_{mag} , which are key quantities for the identification of QCPs and diverge with specific power laws. Experimentally, we found a T^{-1} divergence for Γ_{mag} and Γ_{th} as expected for a BEC QCP. Moreover, we estimated the influence of pressure on the transition temperature T_N and the critical field, H_{c1} and found opposite effects for uniaxial pressure along the crystallographic a and c axes. Uniaxial pressure along the c (a) direction increases (reduces) the ordering temperature T_N , while it reduces (increases) the critical field H_{c1} . Due to the quasi-one-dimensional character of the exchange interactions in DTN, the application of hydrostatic pressure increases T_N and reduces H_{c1} . Our results encourage pressure experiments that shift H_{c1} to zero field. Since the field-induced QCP is BEC-like, the pressure-induced QCP should belong to the $O(2)$ universality class in dimension $D = 3 + z = 3 + 1$ [$z = 1$ for the $O(2)$ QCP].

ACKNOWLEDGMENTS

F.W. was funded by the MPG Research initiative: *Materials Science and Condensed Matter Research at the Hochfeldmagnetlabor Dresden*. M.J. acknowledges hospitality at the MPI for Chemical Physics of Solids, where the experiments were carried out. V.S.Z. acknowledges funding via LDRD/DR Project No. 20100043DR and L.P. was partially supported by CONACyT.

- ¹T. Matsubara and H. Matsuda, *Prog. Theor. Phys.* **16**, 569 (1956).
²E. G. Batyev and L. S. Braginskii, *Zh. Eksp. Teor. Fiz.* **87**, 1361 (1984) [*Sov. Phys.-JETP* **60**, 781 (1984)].
³C. D. Batista and G. Ortiz, *Phys. Rev. Lett.* **86**, 1082 (2001).
⁴C. D. Batista and G. Ortiz, *Adv. Phys.* **53**, 1 (2004).
⁵T. Nikuni, M. Oshikawa, A. Oosawa, and H. Tanaka, *Phys. Rev. Lett.* **84**, 5868 (2000).
⁶T. Giamarchi, C. Rüegg, and O. Tchernyshyov, *Nat. Phys.* **4**, 198 (2008).
⁷V. S. Zapf, M. Jaime, and C. D. Batista, *Rev. Mod. Phys.* (to be published).
⁸A. Paduan-Filho, R. D. Chirico, K. O. Joungh, and R. L. Carlin, *J. Chem. Phys.* **74**, 4103 (1981).
⁹S. A. Zvyagin, J. Wosnitzer, C. D. Batista, M. Tsukamoto, N. Kawashima, J. Krzystek, V. S. Zapf, M. Jaime, N. F. Oliveira Jr., and A. Paduan-Filho, *Phys. Rev. Lett.* **98**, 047205 (2007).
¹⁰L. Yin, J. S. Xia, V. S. Zapf, N. S. Sullivan, and A. Paduan-Filho, *Phys. Rev. Lett.* **101**, 187205 (2008).
¹¹L. Zhu, M. Garst, A. Rosch, and Q. Si, *Phys. Rev. Lett.* **91**, 066404 (2003).
¹²M. Garst and A. Rosch, *Phys. Rev. B* **72**, 205129 (2005).
¹³R. Küchler, N. Oeschler, P. Gegenwart, T. Cichorek, K. Neumaier, O. Tegus, C. Geibel, J. A. Mydosh, F. Steglich, L. Zhu, and Q. Si, *Phys. Rev. Lett.* **91**, 066405 (2003).
¹⁴K. Takatsu, W. Shiramura, and H. Tanaka, *J. Phys. Soc. Jpn.* **66**, 1611 (1997).
¹⁵B. R. Patyal, B. L. Scott, and R. D. Willett, *Phys. Rev. B* **41**, 1657 (1990).
¹⁶A. Oosawa, M. Ishii, and H. Tanaka, *J. Phys.: Condens. Matter.* **11**, 265 (1999).

- ¹⁷B. C. Watson, V. N. Kotov, M. W. Meisel, D. W. Hall, G. E. Granroth, W. T. Montfrooij, S. E. Nagler, D. A. Jensen, R. Backov, M. A. Petruska, G. E. Fanucci, and D. R. Talham, *Phys. Rev. Lett.* **86**, 5168 (2001).
¹⁸T. Lorenz, S. Stark, O. Heyer, N. Hollmann, A. Vasiliev, A. Oosawa, and H. Tanaka, *J. Magn. Magn. Mater.* **316**, 291 (2007).
¹⁹T. Lorenz, O. Heyer, M. Garst, F. Anfuso, A. Rosch, C. Rüegg, and K. Krämer, *Phys. Rev. Lett.* **100**, 067208 (2008).
²⁰V. S. Zapf, V. F. Correa, C. D. Batista, T. P. Murphy, E. D. Palm, M. Jaime, S. Tozer, A. Lacerda, and A. Paduan-Filho, *J. Appl. Phys.* **101**, 09E106 (2007).
²¹A. Paduan-Filho, X. Gratens, and N. F. Oliveira Jr., *Phys. Rev. B* **69**, 020405(R) (2004).
²²T. Sakakibara, H. Mitamura, T. Tayama, and H. Amitsuka, *Jpn. J. Appl. Phys.* **33**, 5067 (1994).
²³R. Pott and R. Scheffzyk, *J. Phys. E: Sci. Instrum.* **16**, 444 (1983).
²⁴H. Wilhelm, T. Lühmann, T. Rus, and F. Steglich, *Rev. Sci. Instrum.* **75**, 2700 (2004).
²⁵S. Riegel and G. Weber, *J. Phys. E: Sci. Instrum.* **19**, 790 (1986).
²⁶See, for instance A. A. Abrikosov, L. P. Gorkov, and I. E. Dzyaloshinskii, *Methods of Quantum Field Theory in Statistical Physics* (Dover, New York, 1975).
²⁷Y. Kohama, A. V. Sologubenko, N. R. Dilley, V. S. Zapf, M. Jaime, J. A. Mydosh, A. Paduan-Filho, K. A. Al-Hassanieh, P. Sengupta, S. Gangadharaiah, A. L. Chernyshev, and C. D. Batista, *Phys. Rev. Lett.* **106**, 037203 (2011).
²⁸A. W. Sandvik and J. Kurkijärvi, *Phys. Rev. B* **43**, 5950 (1991); A. W. Sandvik, *ibid.* **56**, 11678 (1997).
²⁹A. W. Sandvik, *Phys. Rev. B* **59**, R14157 (1999).

- ³⁰O. F. Syljuåsen and A. W. Sandvik, *Phys. Rev. E* **66**, 046701 (2002).
- ³¹K. Hukushima, H. Takayama, and K. Nemoto, *Int. J. Mod. Phys. C* **7**, 337 (1996); K. Hukushima and K. Nemoto, *J. Phys. Soc. Jpn.* **65**, 1604 (1996).
- ³²E. Marinari, in *Advances in Computer Simulation: Lectures Held at the Eötvös Summer School in Budapest*, Hungary, 16-20, July 1996, Lecture Notes in Physics, Vol. 501, edited by J. Kertsz and I. Kondor (Springer, Berlin, 1998).
- ³³P. Sengupta, A. W. Sandvik, and D. K. Campbell, *Phys. Rev. B* **65**, 155113 (2002).
- ³⁴P. Sengupta, A. W. Sandvik, and R. R. P. Singh, *Phys. Rev. B* **68**, 094423 (2003).
- ³⁵V. S. Zapf, D. Zocco, B. R. Hansen, M. Jaime, N. Harrison, C. D. Batista, M. Kenzelmann, C. Niedermayer, A. Lacerda, and A. Paduan-Filho, *Phys. Rev. Lett.* **96**, 077204 (2006).
- ³⁶E. S. R. Gopal, *Specific Heats at Low Temperatures* (Plenum, New York, 1966).
- ³⁷A. Paduan-Filho, X. Gratens, and N. F. Oliveira Jr., *J. Appl. Phys.* **95**, 7537 (2004).
- ³⁸V. S. Zapf, V. F. Correa, P. Sengupta, C. D. Batista, M. Tsukamoto, N. Kawashima, P. Egan, C. Pantea, A. Migliori, J. B. Betts, M. Jaime, and A. Paduan-Filho, *Phys. Rev. B* **77**, 020404(R) (2008); F. Weickert, R. Kuchler, V. Zapf, M. Jaime, and A. Paduan-Filho, *ibid.* **83**, 099901(E) (2011).
- ³⁹O. Chiatti, A. Sytcheva, J. Wosnitza, S. Zherlitsyn, A. A. Zvyagin, V. S. Zapf, M. Jaime, and A. Paduan-Filho, *Phys. Rev. B* **78**, 094406 (2008).
- ⁴⁰F. Weickert, M. Brando, F. Steglich, P. Gegenwart, and M. Garst, *Phys. Rev. B* **81**, 134438 (2010) and references therein.
- ⁴¹N. Johannsen, A. Vasiliev, A. Oosawa, H. Tanaka, and T. Lorenz, *Phys. Rev. Lett.* **95**, 017205 (2005).